iScience

CellPress
OPEN ACCESS

Article

Continuous batch synthesis with atmospheric-pressure microwave plasmas

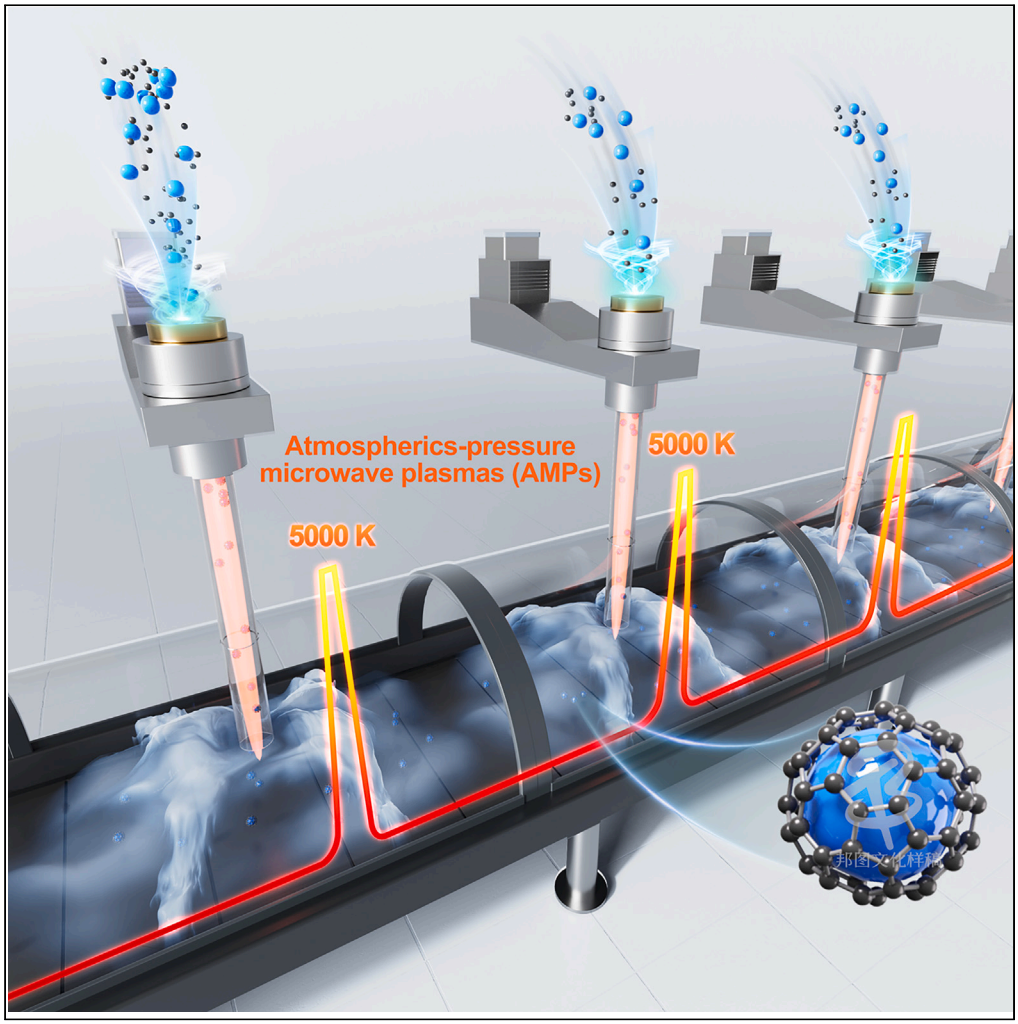

Ziyao Jie, Tian-Yu Wang, Shiyang Huang, Xinpeng Bai, Wenhui Ma, Guixin Zhang, Nan Luo

guixin@mail.tsinghua.edu.cn

Highlights

An electrodeless, high-temperature atmospheric microwave plasma (AMP) was introduced

AMP efficiently synthesized various nanoparticles within tens of milliseconds

The heat impulse can assess plasma characteristics in high-temperature synthesis

Jie et al., iScience *27*, 110328
August 16, 2024 © 2024
Published by Elsevier Inc.
https://doi.org/10.1016/j.isci.2024.110328

iScience

CellPress
OPEN ACCESS

Article

Continuous batch synthesis with atmospheric-pressure microwave plasmas

Ziyao Jie,[1] Tian-Yu Wang,[1,3] Shiyang Huang,[2] Xinpeng Bai,[1] Wenhui Ma,[1] Guixin Zhang,[1,4,*] and Nan Luo[1]

SUMMARY

Plasmas under atmospheric pressure offer a high-temperature environment for material synthesis, but electrode ablation compromises purity. Here, we introduce an atmospheric-pressure microwave plasma (AMP) operated without electrodes to overcome the existing limitations in pure material synthesis. The distribution of the electrostatic field intensity inside a waveguide during AMP excitation was examined via electrostatic field simulations. The lateral and radial gas temperature distributions were also studied using optical emission spectroscopy. The AMP exhibited a uniform ultrahigh temperature (9,000 K), a large volume (10^2–10^4 cm^3), and a response time on the millisecond level. AMP efficiently synthesized silicon nanoparticles, graphene, and graphene@Si–Fe core-shell nanoparticles within tens of milliseconds, ensuring purity and size control. We propose the "heat impulse" metric for evaluating the plasma characteristics (n_a, T_g, and t) in material synthesis, extended to other high-temperature plasmas. AMP is compact, cost-effective, and easy to assemble, promising for eco-friendly mass production of pure materials.

INTRODUCTION

Multiple advanced material synthesis processes necessitate precise conditions: a uniform high temperature (>3,000 K), a rapid heating rate (10^3 K/ms), and a large volume.[1–3] The utilization of plasma has emerged as a promising method because of its enhanced reactivity and lower environmental risks compared to traditional approaches.[4–6] However, fulfilling the simultaneous requirements of a high temperature, a large volume, and a lack of contamination remains a challenge for most plasma technologies. For example, although dielectric barrier discharge, corona, and glow plasmas provide extensive discharge areas, they face limitations due to their modest gas temperatures ($T_g \approx 300$ K), which hinder high-temperature synthesis.[7–10] Various arc plasmas offer an extremely high T_g exceeding 10,000 K and a large plasma volume.[11–13] Nevertheless, these advantages come at the expense of substantial energy consumption and noticeable electrode erosion. Low-temperature plasmas, thermal arc plasmas, and emerging plasmas with diverse discharge structures all share a common feature—the incorporation of electrodes.[1,2,14] Electrode ablation, which is particularly prevalent in high-temperature arc plasmas, leads to a limited duration of plasma sustainment and permanent material contamination.

Because a microwave plasma is generated by a microwave electric field, it inherently has self-ignition and self-sustaining capabilities. Various microwave resonators have been designed to produce uniform microwave plasma under low-pressure conditions.[15–18] However, achieving self-generated uniform microwave plasma without electrodes under atmospheric pressure conditions is an enduring challenge that has not been overcome to date.[19–22]

In this study, we report an ultrahigh-temperature (up to 9,000 K), large-volume (10^2–10^4 cm^3), atmospheric-pressure microwave plasma (AMP) that operates entirely in the absence of electrodes. This particular AMP exhibits a rapid temporal temperature gradient (10^3 K/ms) and can generate various gas-phase environments for various material synthesis and modification applications.

RESULTS AND DISCUSSION

Gas temperature distribution

The AMP virtually reaches the local thermodynamic equilibrium due to lower convection rates compared to those of chemical processes.[23–25] In this case, the heavy species in the atmospheric plasma efficiently interchange both rotational and translational energy.[26] The optical emission spectra (306–310 nm) of OH radicals can be used to determine the gas temperature in the plasma core, and thermocouples can be used to measure the gas temperature in the outer plasma shell outside the waveguide. The gas temperature distribution of the AMP within the waveguide exhibits a consistently stable, large-volume, and uniformly high temperature in the center, as shown in Figure 1C. With an

[1]Department of Electrical Engineering, Tsinghua University, Beijing 100084, China
[2]State Grid Jibei Electric Power Co., Ltd, Research Institute (North China Electric Power Research Institute Co., Ltd, Beijing 100045, China
[3]Department of Chemical and Biomolecular Engineering, University of California, Los Angeles, Los Angeles, CA 90095, USA
[4]Lead contact
*Correspondence: guixin@mail.tsinghua.edu.cn
https://doi.org/10.1016/j.isci.2024.110328

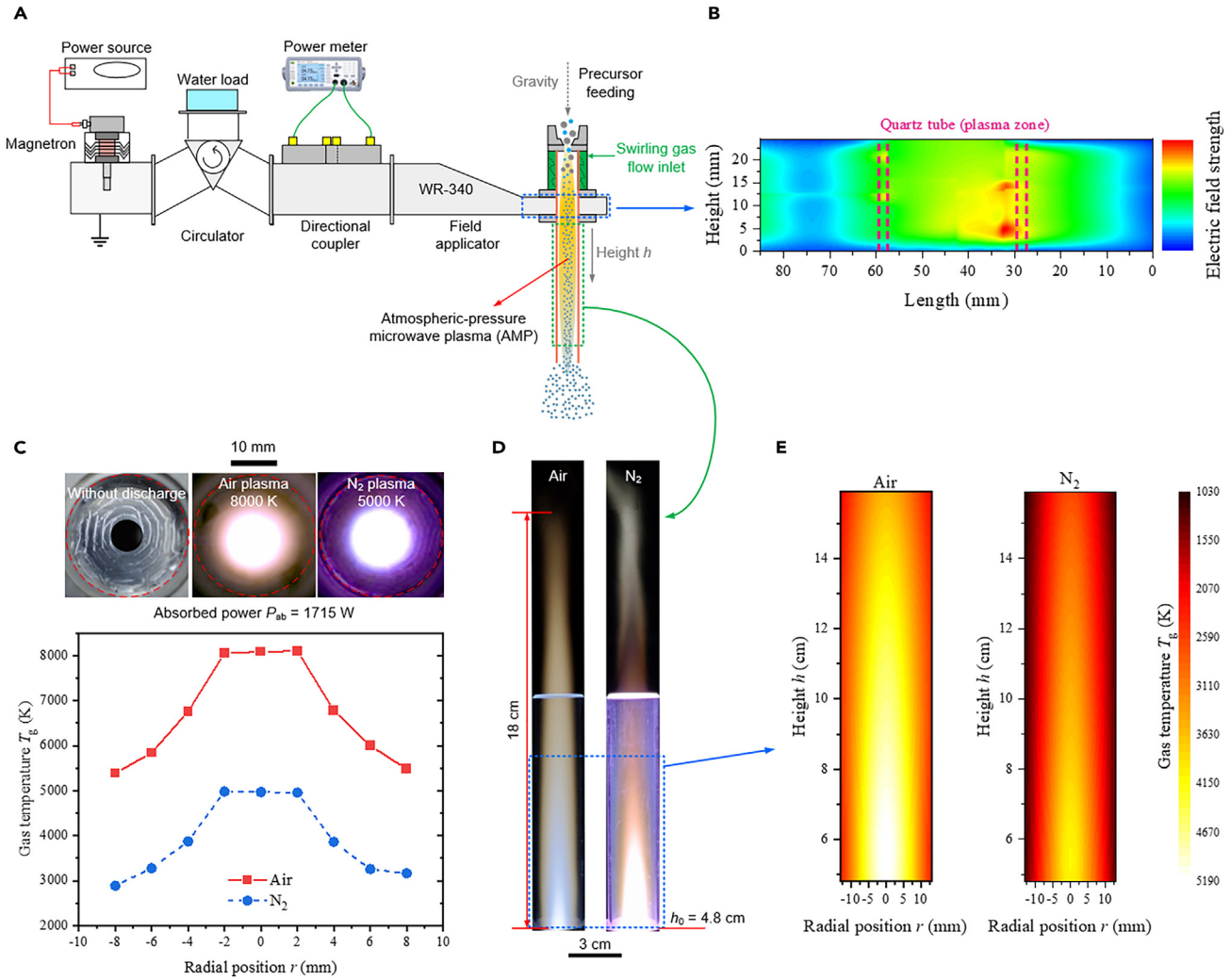

Figure 1. Ultrahigh-temperature, large-volume, and uniform AMP operated without electrodes

(A–E) Schematic of the AMP system; (B) electrostatic field distribution in the compressed waveguide segment that transverses the quartz tube center (highlighted in the blue dotted box in Figure 1A); (C) high-speed images and radial gas temperature distributions measured from the bottom view of the air and N_2 AMPs within the waveguide, showing a uniformly high-temperature area in the plasma core within the waveguide; (D) side views of a section of the air and N_2 AMPs (highlighted in the green dotted box in Figure 1A); and (E) gas temperature contour plots of the air and N_2 AMPs.

absorbed microwave power of 1,715 W, the core regions of the air and N_2 AMPs reach uniformly high temperatures of 8,000 and 5,000 K, respectively. These uniformly high-temperature regions reach the dimensions of approximately $\pi \times (2\ mm)^2 \times 23$ mm in the plasma core within the waveguide. Figure 1E shows the two-dimensional gas temperature contour plots of the AMPs in the region marked by the blue dotted box in Figure 1D. Outside the waveguide, the gas temperature gradually decreases along the axial and radial directions away from the plasma core. The microwave energy density outside the waveguide was relatively low, making the gas temperatures (Figure 1E) in this area lower than the gas temperatures (Figure 1C) of the plasma core inside the waveguide. Additionally, within the range from 8 to 20 L/min, the gas flow rate has a minimal influence on the gas temperature while primarily impacting the dimensions and volume of the AMP. The plasma volume (10^2–10^4 cm^3) and gas temperature (2,000–9,000 K) can be easily controlled (with a millisecond response) by altering the absorption power, gas flow rate, and carrier gas composition. This allows the specific conditions needed for the synthesis of various materials to be met. Furthermore, ultrahigh-temperature and large-volume AMP can remain stable for more than 1 h without water cooling. The introduction of water further extends this duration, allowing for stability throughout the entire lifespan of the magnetron to surpass 1,000 h.

Heat impulse *H*

The AMP in the material synthesis generates a substantial high-temperature area, which is primarily responsible for the presence of neutral particles. Put simply, the properties of the plasma that play a significant role in material synthesis are primarily manifested in the density n_a and

temperature T_g of the neutral particles and the residence time (plasma processing duration) t. The residence time t, which is the duration over which nanomaterials transverse the plasma, can be estimated by dividing the axial length of the plasma by the mean gas flow velocity (details in the supplementary material). According to the results of the confirmatory experiments of this study, the residence time t ranges from 45 to 80 ms, indicating the ultrafast synthesis of nanomaterials by the AMP. According to Dalton's theory, n_a exhibits an inverse relationship with T_g under atmospheric pressure.[22] Hence, the influence of the plasma on the material synthesis process can be ascribed to the joint impact of the gas temperature T_g and processing duration t. Similar to the notion of an impulse, we introduce the concept of the heat impulse $H = T_g \times t$ (Figure 2G) to thoroughly and quantitatively assess the plasma characteristic parameters (n_a, T_g, and t) in the high-temperature synthesis of materials. Furthermore, because the heat impulse H is an inherent characteristic of plasma, it can be used to assess plasma properties under various external conditions. This metric can also be extended to assess various forms of high-temperature (>2,000 K) plasmas for comparison of their properties across various plasmas.

Characterization and properties of the product nanoparticles

A scanning electron microscopy (SEM) image of the produced Si nanoparticles is shown in Figure 2B. The particle diameter distribution was evaluated from multiple SEM images (>10) and is shown in Figure 2C. The Gaussian fit of this distribution yields a mean particle diameter of 17 nm and a narrow full width at half maximum (FWHM) of 15 nm for the Si nanoparticles. The size of the Si nanoparticles exhibits minimal variation across the heat impulse H range from 240 to 380 Ks, and the average particle size remains consistent within the range from 10 to 35 nm, as shown in Figure 2D, demonstrating excellent homogeneity in terms of the particle size achieved using the AMP. The quality of this particle size is on par with the greatest level attained with plasma-enhanced chemical vapor deposition (PECVD) under harsh reaction conditions.[27] In other words, the reaction conditions needed to produce nanoparticles using microwave plasma are quite mild, which is beneficial for industrial production applications. The AMP can also ensure that the silicon particles are smaller than 150 nm, as shown in Figure S2, thus ensuring cycling stability when these particles are used as a lithium battery anode material.[28] Due to the limited magnification in the SEM statistical analysis, many extremely small particles cannot be counted; hence, the AMP approach yields better particle sizes.

"Fluffy" graphene (Figure 2E) can be immediately formed from gas-phase plasma without any catalyst, similar to snowfall, during the plasma cracking of waste polyethylene (PE). As shown from the Raman spectra presented in Figure 2F, the relative intensity ratios I_D/I_G and I_{2D}/I_G are 0.79 and 0.72, respectively, indicating few-layer graphene with abundant defects. This defect-rich and few-layer graphene can provide ample effective Li storage sites and can form a stable solid electrolyte interface during anode cycling.[29,30]

The composite core-shell nanoparticles fabricated using AMP are depicted in Figures 2H–2J. The X-ray diffraction (XRD) pattern suggests that the nanoparticles consist of crystalline iron, silicon, an iron-silicon alloy, and graphite. The Scherrer particle sizes of the silicon (with evident peaks at 28.3°, 47.2°, and 56.0°), iron (with a peak at 44.5°), and ferrosilicon alloy (with a peak near 43.46°) nanoparticles were determined to be 33.9, 9.9, and 6.7 nm, respectively. A high-resolution transmission electron microscopy (HRTEM) image of the nanoparticles generated throughout the high-temperature AMP is shown in Figure 2I. The mean interplanar spacings within the regions marked by the red, green, blue, and magenta boxes in Figure 2I are consistent with the (220) crystallographic plane of Si, the (002) plane of graphene, the (110) plane of Fe, and the distinctive plane characterizing the Fe-Si alloy, respectively, as shown in Figures S3 and S4. These findings reveal that the nanoparticles synthesized using the AMP consist of an amalgamation of an iron-silicon alloy, silicon nanoparticles, and iron nanoparticles embedded within the layered structure of graphene. The formation of this structure is a consequence of the violent collisions between the particles induced by the high-frequency microwave electromagnetic field and high temperatures in the AMP. These impacts promote inelastic interactions between the individual silicon and iron particles, leading to partial alloy formation and ultimately the formation of these composite entities. In addition, we investigated the impact of various plasma characteristic parameter (heat impulse H) conditions and the silicon concentration in the precursor on the particle size and coating of this composite material, as shown in Figures 2J, S5, and S6. AMP (H ranging from 240 to 380 Ks) can be utilized to produce core-shell nanoparticles with precise and consistent particle sizes (20–40 nm), as shown in Figure 2J; this approach is superior to other methods (e.g., deflagration, hydrogel methods, and polymerization restriction).[3,31–33] The coating ratio of the composite particles with graphene decreases with an increasing proportion of the silicon source in the precursor, as shown in Figure S5. Notably, at an approximate silicon source proportion of 40%, the coating ratio reaches 90%, as shown in Figure S5. Unlike the core-shell nanoparticles generated via other methods (e.g., arc plasma, electrostatic attraction, aerosol, and hydrothermal synthesis), the nanoparticles obtained by using the AMP are extremely pure and small and do not contain oxygen-containing functional groups in the graphene layer shell, which is a problem encountered when using other synthesis methods.[31,32,34–37]

Indeed, AMP ($H > 10^4$ Ks) can also serve as a means for producing bulk materials with larger size. For instance, inorganic fly ash and glass waste can be sintered with AMP into a vitreous (amorphous) body in an open atmosphere, as shown in Figure S7. In brief, nanoparticles can be prepared using an AMP with a minor heat impulse, and bulk materials that require high temperatures can be synthesized by employing an AMP with a much greater heat impulse that can be achieved by altering the processing technique to extend the residence time.

Comparison to other techniques

Compared with other nonthermal equilibrium plasmas and PECVD,[8–10,38–45] as shown in Figure 3A, an AMP can produce extremely high (up to 9,000 K), uniform, and stable gas temperatures over a large volume (10^2–10^4 cm^3) for a long time with a modest power input (e.g., 0.5–2 kW). AMPs whose gas temperatures reach several thousand degrees can rapidly induce vaporization or melting of materials, hence facilitating the processes of melting, sintering, or nanomaterial preparation. By contrast, PECVD and low-temperature plasmas, such as dielectric barrier discharge, corona, and glow plasmas, cannot carry out this task and can only treat the surface. Unlike arc (including gliding arc) plasmas,

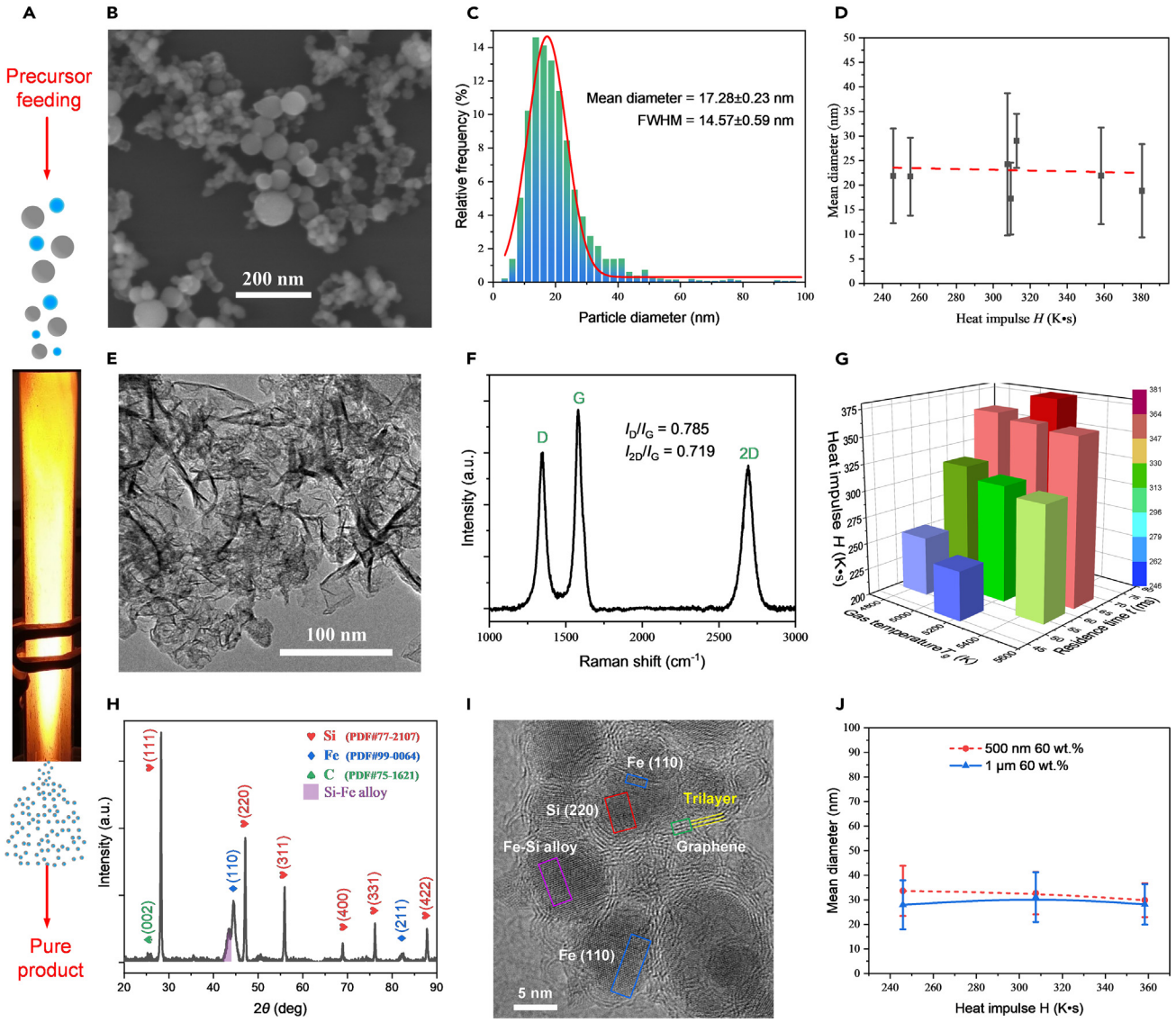

Figure 2. Application of an N_2 AMP in the synthesis of various nanomaterials

(A–J) Schematic of the practical process of material preparation using an AMP; (B) an SEM image of Si nanoparticles synthesized from micron-scale silicon using an AMP; (C) influence of heat impulse *H* on the size distribution of Si nanoparticles in the SEM images of the Si nanoparticles synthesized using an AMP; (D) influence of heat impulse *H* on the Gaussian mean Si particle size and its FWHM; (E) a transmission electron microscopy (TEM) image of graphene synthesized from waste high-density PE using an AMP; (F) Raman spectra of graphene synthesized from waste high-density PE using an AMP; (G) 3D schematic illustrating the dependence of heat impulse *H* on gas temperature T_g and residence time *t*; (H) XRD pattern of graphene@Si–Fe nanoparticles synthesized using an AMP; (I) HRTEM image of graphene@Si–Fe nanoparticles synthesized using an AMP; and (J) influence of heat impulse *H* on the Gaussian mean graphene@Si–Fe particle size and its FWHM.

the AMP is characterized by its electrodeless nature, eliminating the issues of electrode ablation and material contamination.[12,13,39–42,46,47] Hence, microwave plasma can generate highly refined materials that can be applied in a variety of fields. Moreover, AMP can function at low power levels (e.g., 0.5–2 kW). By contrast, arc plasma requires a minimum driving power of 50 kW,[48,49] which inevitably results in large energy losses during material synthesis, as the system must be equipped with an effective cooling system to handle this high energy input.

Despite the significant benefits of the PECVD method in generating high-quality nanomaterials, it is plagued by issues such as a low-pressure working environment, the use of complex equipment, extremely high cost, and the use of flammable and explosive raw ingredients (e.g., hydrogen, alkanes, and silane). The viability of industrial-scale continuous production based on PECVD is constrained by these issues, which can be effectively addressed through the use of the AMP technique.[27,44,58,59] AMPs can offer lower energy consumption and lower costs for scalable syntheses of nanomaterials and facilities; therefore, they are suitable for industrial applications.

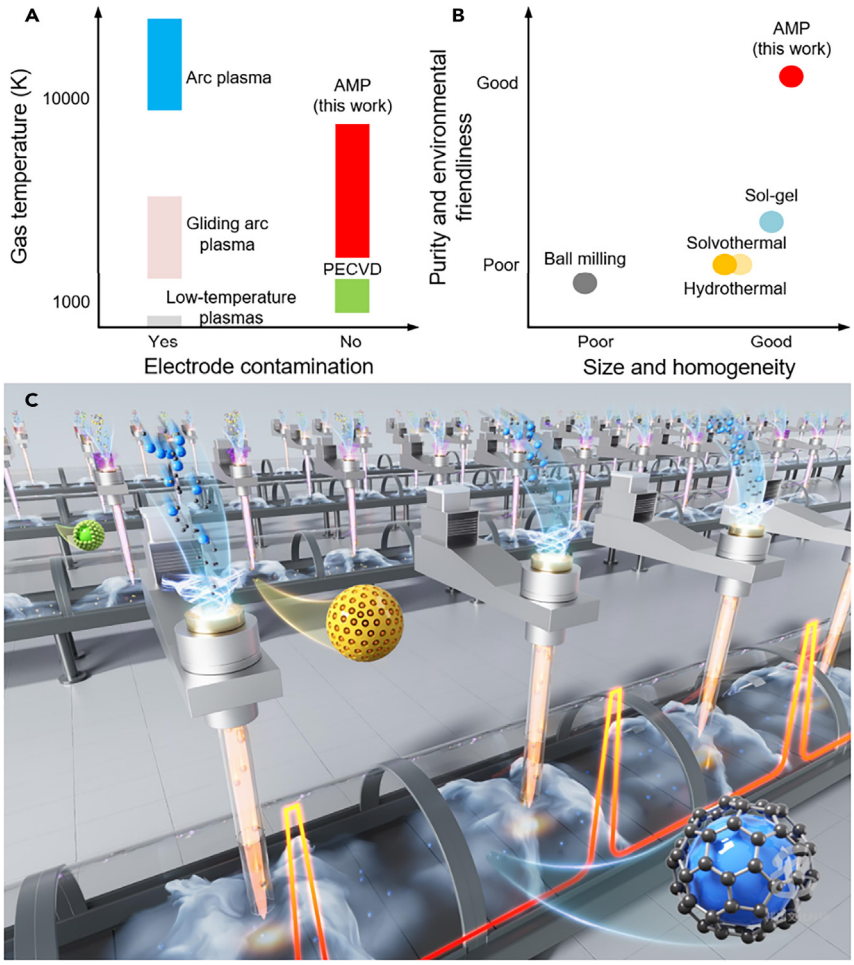

Figure 3. Technique comparison and future prospects of AMP in material synthesis

(A and B) Comparison of the gas temperature and electrode contamination of AMP with those of other plasmas,[8–10,12,13,38–47] revealing the advantage of AMP in generating ultrahigh temperatures without electrode ablation; (B) comparison of the purity and environmental friendliness of AMP and the size and homogeneity of the synthesized nanoparticles with those of other techniques[32,50–57]; and (C) mass production prospects for AMP modules in continuous batch synthesis of materials.

Production of pure product materials by ball milling and chemical synthesis techniques (e.g., sol-gel, hydrothermal, and solvothermal techniques) is difficult due to the limitations in chemical reagents (Figure 3B).[32,50–57] Additionally, some chemicals are not environmentally friendly. The AMP approach effectively mitigates contamination issues inherent to these conventional methods. The AMP method excels in the production of nanomaterials. For example, AMP can produce high-quality silicon nanoparticles with an average particle size of 17–30 nm and a particle size distribution width of 10–20 nm without requiring a harsh reaction environment. The AMP approach outperforms hydrothermal, sol-gel, and other chemical processes in terms of the quality of the resulting particles, including their size and homogeneity. Moreover, this approach achieves a particle size quality comparable to that achieved by the best PECVD methods while avoiding the high expense and complexity associated with mass production using chemical vapor deposition methods on an industrial scale.[27,44,58,59]

Conclusions, outlook, and future aspects

AMP driven only by clean electricity provides a fast response (millisecond level), is controllable, and has a uniform high temperature (up to 9,000 K) over a large volume (10^2–10^4 cm^3), making it an efficient solution for industrial mass manufacturing. By determining the operating conditions specific to each process, it becomes feasible to customize waveguides for particular applications. For instance, energy-absorbing and tuning components like circulators, water loads, and three-stub tuners can be excluded from operational conditions based on the requirements of the process, achieved by adjusting the waveguide size (e.g., modifying the distance between the short end and the quartz tube) to achieve optimal resonance or zero-power reflection. The AMP can be seamlessly integrated into a compact module comprising only a cost-effective field applicator and a magnetron, as illustrated in Figure 3C. The absence of a water load, circulator, directional coupler,

and three-stub tuner in the AMP generator is expected to yield space and cost savings in industrial microwave plasma applications. The resulting AMP module demonstrates a remarkable degree of versatility, compactness, and ease of assembly, accommodating a broad range of surroundings and reaction conditions with modest green power consumption. Multiple AMP modules can be assembled in parallel (as shown in Figure 3C) or in series based on industrial requirements.

Taking the synthesis of nanosilicon as an example, the reaction time between the precursor and AMP is ultrafast (tens of milliseconds), and a single AMP module offers a productivity of nearly 100 g/h. By arranging 100 modules in parallel, the productivity can reach approximately 10 kg/h. Since microwave plasma is a dry preparation process, it can significantly reduce the overall process cost compared to chemical wet processes. Assuming that the electricity price is 1 Chinese yuan/kWh and the power of the microwave plasma source module is 2 kW, the plasma energy consumption cost of 100 microwave plasma modules running at the same time to prepare nanosilicon particles is only ~18 Chinese yuan/kg. Comparison with the cost of current commercially available 20 nm silicon particles, which is 24,900 Chinese yuan/kg, shows that the microwave plasma dry preparation method and its relaxed reaction conditions can provide rapid and low-cost preparation capabilities for nanomaterials; thus, this method is expected to contribute to the development of high-temperature nanomaterials. Large-scale production provides clean, green, and efficient solutions with broad commercial prospects. Every module has the capability to function continuously for more than 40 days using renewable electricity only.

This flexibility allows for the utilization of AMP in various processes, such as continuous material synthesis, surface modification, or powder bed fusion-sintering processes in industrial production lines, as depicted in Figure 3C. In addition, the dry AMP process and mild reaction conditions enable the realization of rapid synthesis (e.g., 50 ms) while eliminating solvents and reducing the overall cost. As a result, AMP can provide a clean, green, and efficient solution for the mass production of high-temperature materials.

Limitations of the study

Various collection techniques can influence the cooling, separation, and agglomeration of nanomaterials, warranting further examination.

STAR★METHODS

Detailed methods are provided in the online version of this paper and include the following:

- KEY RESOURCES TABLE
- RESOURCE AVAILABILITY
  - Lead contact
  - Materials availability
  - Data and code availability
- EXPERIMENTAL MODEL AND SUBJECT DETAILS
  - AMP generator
  - Materials and conditions
- METHOD DETAILS
  - Gas temperature measurement
  - Residence time estimation

SUPPLEMENTAL INFORMATION

Supplemental information can be found online at https://doi.org/10.1016/j.isci.2024.110328.

ACKNOWLEDGMENTS

This work was supported by the National Natural Science Foundation of China (grant no. 51176098) and the Beijing Science and Technology Planning Project (grant no. Z191100002019014). Special appreciation is extended to Dr. Yang Min from the School of Vehicle and Mobility at Tsinghua University for invaluable insights into the material synthesis and characterization.

AUTHOR CONTRIBUTIONS

Conceptualization, Z.J. and G.Z.; methodology, Z.J.; software, S.H. and Z.J.; validation, Z.J., X.B., and W.M.; formal analysis, Z.J. and S.H.; investigation, Z.J., X.B., W.M., and N.L.; resources, T.-Y.W. and G.Z.; writing – original draft, Z.J.; writing – review and editing, Z.J., T.-Y.W., S.H., and G.Z.; supervision, G.Z.; funding acquisition, G.Z.

DECLARATION OF INTERESTS

The authors declare no competing interests.

Received: January 15, 2024
Revised: May 28, 2024
Accepted: June 18, 2024
Published: June 29, 2024

REFERENCES

1. Xie, H., Liu, N., Zhang, Q., Zhong, H., Guo, L., Zhao, X., Li, D., Liu, S., Huang, Z., Lele, A.D., et al. (2023). A stable atmospheric-pressure plasma for extreme-temperature synthesis. Nature *623*, 964–971. https://doi.org/10.1038/s41586-023-06694-1.
2. Dou, S., Tao, L., Wang, R., El Hankari, S., Chen, R., and Wang, S. (2018). Plasma-Assisted Synthesis and Surface Modification of Electrode Materials for Renewable Energy. Adv. Mater. *30*, e1705850. https://doi.org/10.1002/adma.201705850.
3. Yang, M., Liu, J., Li, S., Zhang, S., Wang, Y., and He, C. (2019). Ultrafast synthesis of graphene nanosheets encapsulated Si nanoparticles via deflagration of energetic materials for lithium-ion batteries. Nano Energy *65*, 104028. https://doi.org/10.1016/j.nanoen.2019.104028.
4. Schwenke, A.M., Hoeppener, S., and Schubert, U.S. (2015). Synthesis and Modification of Carbon Nanomaterials utilizing Microwave Heating. Adv. Mater. *27*, 4113–4141. https://doi.org/10.1002/adma.201500472.
5. Li, K., Jiang, Q., Chen, G., Gao, L., Peng, J., Chen, Q., Koppala, S., Omran, M., and Chen, J. (2021). Kinetics characteristics and microwave reduction behavior of walnut shell-pyrolusite blends. Bioresour. Technol. *319*, 124172. https://doi.org/10.1016/j.biortech.2020.124172.
6. Kortshagen, U.R., Sankaran, R.M., Pereira, R.N., Girshick, S.L., Wu, J.J., and Aydil, E.S. (2016). Nonthermal Plasma Synthesis of Nanocrystals: Fundamental Principles, Materials, and Applications. Chem. Rev. *116*, 11061–11127. https://doi.org/10.1021/acs.chemrev.6b00039.
7. Brandenburg, R. (2017). Dielectric barrier discharges: progress on plasma sources and on the understanding of regimes and single filaments. Plasma Sources Sci. Technol. *26*, 053001. https://doi.org/10.1088/1361-6595/aa6426.
8. Schutze, A., Jeong, J.Y., Babayan, S.E., Jaeyoung, P., Selwyn, G.S., and Hicks, R.F. (1998). The atmospheric-pressure plasma jet: a review and comparison to other plasma sources. IEEE Trans. Plasma Sci. *26*, 1685–1694. https://doi.org/10.1109/27.747887.
9. Park, J., Henins, I., Herrmann, H.W., Selwyn, G.S., Jeong, J.Y., Hicks, R.F., Shim, D., and Chang, C.S. (2000). An atmospheric pressure plasma source. ApPhL *76*, 288–290. https://doi.org/10.1063/1.125724.
10. Baránková, H., and Bárdoš, L. (2003). Hollow cathode cold atmospheric plasma source with monoatomic and molecular gases. SuCT *163–164*, 649–653. https://doi.org/10.1016/s0257-8972(02)00688-6.
11. Groger, S., Ramakers, M., Hamme, M., Medrano, J.A., Bibinov, N., Gallucci, F., Bogaerts, A., and Awakowicz, P. (2019). Characterization of a nitrogen gliding arc plasmatron using optical emission spectroscopy and high-speed camera. J. Phys. D-Appl. Phys. *52*, 065201. https://doi.org/10.1088/1361-6463/aaefe4.
12. Murphy, A.B. (2015). A Perspective on Arc Welding Research: The Importance of the Arc, Unresolved Questions and Future Directions. Plasma Chem. Plasma Process. *35*, 471–489. https://doi.org/10.1007/s11090-015-9620-2.
13. Suzuki, R., Matsuoka, Y., Hirotani, D., Nezu, A., Mori, S., and Akatsuka, H. (2021). Spectroscopic Measurement of Arc-Discharge Argon Plasma Plume Injected into Water. IEEJ Transactions Elec. Engng. *16*, 364–373. https://doi.org/10.1002/tee.23305.
14. Khoja, A.H., Mazhar, A., Saleem, F., Mehran, M.T., Naqvi, S.R., Anwar, M., Shakir, S., Saidina Amin, N.A., and Sajid, M.B. (2021). Recent developments in catalyst synthesis using DBD plasma for reforming applications. Int. J. Hydrogen Energy. *46*, 15367–15388. https://doi.org/10.1016/j.ijhydene.2021.02.043.
15. Itarashiki, T., Hayashi, N., and Yonesu, A. (2014). Sterilization effect of nitrogen oxide radicals generated by microwave plasma using air. Vacuu *110*, 213–216. https://doi.org/10.1016/j.vacuum.2014.06.018.
16. Lebedev, Y.A. (2015). Microwave discharges at low pressures and peculiarities of the processes in strongly non-uniform plasma. Plasma Sources Sci. Technol. *24*, 053001. https://doi.org/10.1088/0963-0252/24/5/053001.
17. Zhang, Q., Zhang, G.X., Wang, S.M., and Wang, L.M. (2011). A large-volume microwave plasma source based on parallel rectangular waveguides at low pressures. Plasma Sources Sci. Technol. *20*, 015025. https://doi.org/10.1088/0963-0252/20/1/015025.
18. Kais, A., Lo, J., Therese, L., and Guillot, P. (2018). Heating power at the substrate, electron temperature, and electron density in 2.45 GHz low-pressure microwave plasma. PhPl *25*, 013504. https://doi.org/10.1063/1.5005592.
19. Baeva, M., Andrasch, M., Ehlbeck, J., Loffhagen, D., and Weltmann, K.D. (2014). Temporally and spatially resolved characterization of microwave induced argon plasmas: Experiment and modeling. J. Appl. Phys. *115*, 143301. https://doi.org/10.1063/1.4870858.
20. Zhang, S., Chen, Z., Yang, J., Chen, S., Feng, D., Zhou, Y., Wang, B., and Lu, X. (2021). Study on discharge mode and transition mechanism of atmospheric pressure Ar/Zn pulsed microwave plasma jet. AIP Adv. *11*, 095201. https://doi.org/10.1063/5.0060269.
21. Snirer, M., Toman, J., Kudrle, V., and Jasek, O. (2021). Stable filamentary structures in atmospheric pressure microwave plasma torch. Plasma Sources Sci. Technol. *30*, 095009. https://doi.org/10.1088/1361-6595/ac1ee0.
22. Leins, M., Walker, M., Schulz, A., Schumacher, U., and Stroth, U. (2012). Spectroscopic Investigation of a Microwave-Generated Atmospheric Pressure Plasma Torch. Contrib. Plasm. Phys. *52*, 615–628. https://doi.org/10.1002/ctpp.201210058.
23. Laux, C.O., Spence, T.G., Kruger, C.H., and Zare, R.N. (2003). Optical diagnostics of atmospheric pressure air plasmas. Plasma Sources Sci. Technol. *12*, 125–138. https://doi.org/10.1088/0963-0252/12/2/301.
24. Jie, Z., Liu, C., Huang, S., and Zhang, G. (2021). Mechanisms of gas temperature variation of the atmospheric microwave plasma torch. J. Appl. Phys. *129*, 233302. https://doi.org/10.1063/5.0049620.
25. Jie, Z., Liu, C., Xia, D., Zhang, Z., Zhao, X., and Zhang, G. (2023). Determination of 915-MHz Atmospheric Pressure Air Microwave Plasma Torch (MPT) Parameters. IEEE Trans. Plasma Sci. *51*, 456–465. https://doi.org/10.1109/TPS.2023.3236689.
26. Bruggeman, P., Iza, F., Guns, P., Lauwers, D., Kong, M.G., Gonzalvo, Y.A., Leys, C., and Schram, D.C. (2010). Electronic quenching of OH(A) by water in atmospheric pressure plasmas and its influence on the gas temperature determination by OH(A–X) emission. Plasma Sources Sci. Technol. *19*, 015016. https://doi.org/10.1088/0963-0252/19/1/015016.
27. Li, H., Li, H., Lai, Y., Yang, Z., Yang, Q., Liu, Y., Zheng, Z., Liu, Y., Sun, Y., Zhong, B., et al. (2022). Revisiting the Preparation Progress of Nano-Structured Si Anodes toward Industrial Application from the Perspective of Cost and Scalability. Adv. Energy Mater. *12*, 2102181. https://doi.org/10.1002/aenm.202102181.
28. Liu, X.H., Zhong, L., Huang, S., Mao, S.X., Zhu, T., and Huang, J.Y. (2012). Size-dependent fracture of silicon nanoparticles during lithiation. ACS Nano *6*, 1522–1531. https://doi.org/10.1021/nn204476h.
29. Yoo, E., Kim, J., Hosono, E., Zhou, H.S., Kudo, T., and Honma, I. (2008). Large reversible Li storage of graphene nanosheet families for use in rechargeable lithium ion batteries. Nano Lett. *8*, 2277–2282. https://doi.org/10.1021/nl800957b.
30. Hu, J., Li, H., and Huang, X. (2007). Electrochemical behavior and microstructure variation of hard carbon nano-spherules as anode material for Li-ion batteries. SSIon *178*, 265–271. https://doi.org/10.1016/j.ssi.2006.12.014.
31. Bai, X., Yu, Y., Kung, H.H., Wang, B., and Jiang, J. (2016). Si@SiO_x/graphene hydrogel composite anode for lithium-ion battery. J. Appl. Phys. *306*, 42–48. https://doi.org/10.1016/j.jpowsour.2015.11.102.
32. Li, X., Wu, M., Feng, T., Xu, Z., Qin, J., Chen, C., Tu, C., and Wang, D. (2017). Graphene enhanced silicon/carbon composite as anode for high performance lithium-ion batteries. RSC Adv. *7*, 48286–48293. https://doi.org/10.1039/c7ra09818a.
33. Wang, Y., Wang, Y., Hosono, E., Wang, K., and Zhou, H. (2008). The design of a $LiFePO_4$/carbon nanocomposite with a core-shell structure and its synthesis by an in situ polymerization restriction method. Angew. Chem. Int. Ed. Engl. *47*, 7461–7465. https://doi.org/10.1002/anie.200802539.

34. Kim, D.-W., Kim, T.-H., Choi, S., Kim, K.-S., and Park, D.-W. (2012). Preparation of silica coated iron oxide nanoparticles using non-transferred arc plasma. Adv. Powder Technol. *23*, 701–707. https://doi.org/10.1016/j.apt.2011.09.001.
35. Yang, S., Feng, X., Ivanovici, S., and Müllen, K. (2010). Fabrication of Graphene-Encapsulated Oxide Nanoparticles: Towards High-Performance Anode Materials for Lithium Storage. Angew. Chem. *122*, 8586–8589. https://doi.org/10.1002/ange.201003485.
36. Zhou, X., Yin, Y.-X., Wan, L.-J., and Guo, Y.-G. (2012). Self-Assembled Nanocomposite of Silicon Nanoparticles Encapsulated in Graphene through Electrostatic Attraction for Lithium-Ion Batteries. Adv. Energy Mater. *2*, 1086–1090. https://doi.org/10.1002/aenm.201200158.
37. Wen, Y., Zhu, Y., Langrock, A., Manivannan, A., Ehrman, S.H., and Wang, C. (2013). Graphene-bonded and -encapsulated si nanoparticles for lithium ion battery anodes. Small *9*, 2810–2816. https://doi.org/10.1002/smll.201202512.
38. Hubicka, Z., Cada, M., Sícha, M., Churpita, A., Pokorný, P., Soukup, L., and Jastrabík, L. (2002). Barrier-torch discharge plasma source for surface treatment technology at atmospheric pressure. Plasma Sources Sci. Technol. *11*, 195–202. https://doi.org/10.1088/0963-0252/11/2/311.
39. Zhu, F., Zhang, H., Yang, H., Yan, J., Li, X., and Tu, X. (2020). Plasma reforming of tar model compound in a rotating gliding arc reactor: Understanding the effects of CO_2 and H_2O addition. Fuel *259*, 116271. https://doi.org/10.1016/j.fuel.2019.116271.
40. Liu, J.L., Gao, Y., Sun, B., Zhu, B., Li, X.S., and Zhu, A.M. (2022). Mechanism study on gliding arc (GA) plasma reforming: A combination approach of experiment and modeling. Plasma Process. Polym. *19*, 2200077. https://doi.org/10.1002/ppap.202200077.
41. Chun, Y.N., Yang, Y.C., and Yoshikawa, K. (2009). Hydrogen generation from biogas reforming using a gliding arc plasma-catalyst reformer. Catal. Today *148*, 283–289. https://doi.org/10.1016/j.cattod.2009.09.019.
42. Tu, X., and Whitehead, J.C. (2014). Plasma dry reforming of methane in an atmospheric pressure AC gliding arc discharge: Co-generation of syngas and carbon nanomaterials. Int. J. Hydrogen Energy. *39*, 9658–9669. https://doi.org/10.1016/j.ijhydene.2014.04.073.
43. Li, Y., Mann, D., Rolandi, M., Kim, W., Ural, A., Hung, S., Javey, A., Cao, J., Wang, D., Yenilmez, E., et al. (2004). Preferential Growth of Semiconducting Single-Walled Carbon Nanotubes by a Plasma Enhanced CVD Method. Nano Lett. *4*, 317–321. https://doi.org/10.1021/nl035097c.
44. Schwan, J., Nava, G., and Mangolini, L. (2020). Critical barriers to the large scale commercialization of silicon-containing batteries. Nanoscale Adv. *2*, 4368–4389. https://doi.org/10.1039/d0na00589d.
45. Bo, Z., Yang, Y., Chen, J., Yu, K., Yan, J., and Cen, K. (2013). Plasma-enhanced chemical vapor deposition synthesis of vertically oriented graphene nanosheets. Nanoscale *5*, 5180–5204. https://doi.org/10.1039/c3nr33449j.
46. Wang, Q., Yan, J., Tu, X., Chi, Y., Li, X., Lu, S., and Cen, K. (2009). Thermal treatment of municipal solid waste incinerator fly ash using DC double arc argon plasma. Fuel *88*, 955–958. https://doi.org/10.1016/j.fuel.2008.12.011.
47. Gomez, E., Rani, D.A., Cheeseman, C.R., Deegan, D., Wise, M., and Boccaccini, A.R. (2009). Thermal plasma technology for the treatment of wastes: a critical review. J. Hazard Mater. *161*, 614–626. https://doi.org/10.1016/j.jhazmat.2008.04.017.
48. Jie, Z., Liu, C., Xia, D., and Zhang, G. (2023). Microwave plasma torches for solid waste treatment and vitrification. Environ. Sci. Pollut. Res. Int. *30*, 32827–32838. https://doi.org/10.1007/s11356-022-24523-2.
49. Jie, Z., Liu, C., Xia, D., and Zhang, G. (2023). An atmospheric microwave plasma-based distributed system for medical waste treatment. Environ. Sci. Pollut. Res. Int. *30*, 51314–51326. https://doi.org/10.1007/s11356-023-25793-0.
50. Sarwat, S.G. (2017). Contamination in wet-ball milling. Powder Metall. *60*, 267–272. https://doi.org/10.1080/00325899.2017.1280647.
51. Hou, X., Zhang, M., Wang, J., Hu, S., Liu, X., and Shao, Z. (2015). High yield and low-cost ball milling synthesis of nano-flake Si@SiO_2 with small crystalline grains and abundant grain boundaries as a superior anode for Li-ion batteries. J. Alloys Compd. *639*, 27–35. https://doi.org/10.1016/j.jallcom.2015.03.127.
52. Liu, N., Wu, H., McDowell, M.T., Yao, Y., Wang, C., and Cui, Y. (2012). A yolk-shell design for stabilized and scalable li-ion battery alloy anodes. Nano Lett. *12*, 3315–3321. https://doi.org/10.1021/nl3014814.
53. Kim, M.K., Shin, W.H., and Jeong, H.M. (2019). Protective carbon-coated silicon nanoparticles with graphene buffer layers for high performance anodes in lithium-ion batteries. ApSS *467–468*, 926–931. https://doi.org/10.1016/j.apsusc.2018.10.253.
54. Batool, S., Idrees, M., Kong, J., Zhang, J., Kong, S., Dong, M., Hou, H., Fan, J., Wei, H., and Guo, Z. (2020). Assessment of the electrochemical behaviour of silicon@carbon nanocomposite anode for lithium-ion batteries. J. Alloys Compd. *832*, 154644. https://doi.org/10.1016/j.jallcom.2020.154644.
55. Luo, W., Wang, Y., Chou, S., Xu, Y., Li, W., Kong, B., Dou, S.X., Liu, H.K., and Yang, J. (2016). Critical thickness of phenolic resin-based carbon interfacial layer for improving long cycling stability of silicon nanoparticle anodes. Nano Energy *27*, 255–264. https://doi.org/10.1016/j.nanoen.2016.07.006.
56. Wu, W., He, Q., and Jiang, C. (2008). Magnetic iron oxide nanoparticles: synthesis and surface functionalization strategies. Nanoscale Res. Lett. *3*, 397–415. https://doi.org/10.1007/s11671-008-9174-9.
57. Erk, C., Brezesinski, T., Sommer, H., Schneider, R., and Janek, J. (2013). Toward silicon anodes for next-generation lithium ion batteries: a comparative performance study of various polymer binders and silicon nanopowders. ACS Appl. Mater. Interfaces *5*, 7299–7307. https://doi.org/10.1021/am401642c.
58. Source, J., Quinsac, A., Leconte, Y., Sublemontier, O., Porcher, W., Haon, C., Bordes, A., De Vito, E., Boulineau, A., Jouanneau Si Larbi, S., et al. (2015). One-step synthesis of Si@C nanoparticles by laser pyrolysis: high-capacity anode material for lithium-ion batteries. ACS Appl. Mater. Interfaces *7*, 6637–6644. https://doi.org/10.1021/am5089742.
59. Son, I.H., Hwan Park, J., Kwon, S., Park, S., Rummeli, M.H., Bachmatiuk, A., Song, H.J., Ku, J., Choi, J.W., Choi, J.M., et al. (2015). Silicon carbide-free graphene growth on silicon for lithium-ion battery with high volumetric energy density. Nat. Commun. *6*, 7393. https://doi.org/10.1038/ncomms8393.
60. Jie, Z., Zhang, Z., Bai, X., Ma, W., Zhao, X., Chen, Q., and Zhang, G. (2023). Surface-wave-sustained plasma synthesis of graphene@Fe–Si nanoparticles for lithium-ion battery anodes. ApPhL *123*, 113902. https://doi.org/10.1063/5.0159269.
61. Hou, G., Cheng, B., Yang, Y., Du, Y., Zhang, Y., Li, B., He, J., Zhou, Y., Yi, D., Zhao, N., et al. (2019). Multiscale Buffering Engineering in Silicon-Carbon Anode for Ultrastable Li-Ion Storage. ACS Nano *13*, 10179–10190. https://doi.org/10.1021/acsnano.9b03355.
62. Hou, G., Cheng, B., Ding, F., Yao, M., Cao, Y., Hu, P., Ma, R., and Yuan, F. (2015). Well dispersed silicon nanospheres synthesized by RF thermal plasma treatment and their high thermal conductivity and dielectric constant in polymer nanocomposites. RSC Adv. *5*, 9432–9440. https://doi.org/10.1039/c4ra14212h.
63. Kumar, R., Sahoo, S., Joanni, E., Singh, R.K., Yadav, R.M., Verma, R.K., Singh, D.P., Tan, W.K., Pérez del Pino, A., Moshkalev, S.A., and Matsuda, A. (2019). A review on synthesis of graphene, h-BN and MoS_2 for energy storage applications: Recent progress and perspectives. Nano Res. *12*, 2655–2694. https://doi.org/10.1007/s12274-019-2467-8.
64. Wang, T.Y., Li, X.F., Jie, Z., Liu, B.X., Zhang, G., Liu, J.B., Dang, Z.M., and Wang, Z.L. (2023). Polymer Dielectrics with Outstanding Dielectric Characteristics via Passivation with Oxygen Atoms through C-F Vacancy Carbonylation. Nano Lett. *23*, 8808–8815. https://doi.org/10.1021/acs.nanolett.3c01987.
65. Bruggeman, P.J., Sadeghi, N., Schram, D.C., and Linss, V. (2014). Gas temperature determination from rotational lines in non-equilibrium plasmas: a review. Plasma Sources Sci. Technol. *23*, 023001. https://doi.org/10.1088/0963-0252/23/2/023001.
66. ZHAI, X., DING, Y., PENG, Z., CHENG, L., and LUO, R. (2012). Temperature determination of an oxyacetylene flame based on the OH radical emission spectrum. J. Tsinghua. Univ. (Sci. Tech.) *52*, 980–983. https://doi.org/10.16511/j.cnki.qhdxxb.2012.07.004.
67. Luque, J., and Crosley, D.R. (1999). LIFBASE: Database and Spectral Simulation, 2.0. SRI Int. Rep. MP, 99-009.
68. Chen, C.-J., and Li, S.-Z. (2015). Spectroscopic measurement of plasma gas temperature of the atmospheric-pressure microwave induced nitrogen plasma torch. Plasma Sources Sci. Technol. *24*, V. https://doi.org/10.1088/0963-0252/24/3/035017.

STAR★METHODS

KEY RESOURCES TABLE

REAGENT or RESOURCE	SOURCE	IDENTIFIER
Chemicals, peptides, and recombinant proteins		
Silicon powder	China Qinghe County Xintie Metal Materials Co., Ltd.	CAS#7440-21-3
Ferrocene	Shanghai Macklin Biochemical Technology Co., Ltd.	CAS#102-54-5
High-density polyethylene	Shanghai Macklin Biochemical Technology Co., Ltd.	CAS#9002-88-4
Nitrogen gas (99.999%)	Beijing Haipu Beifen Gas Industry Co., Ltd.	CAS#7727-37-9
Software and algorithms		
LIFBASE: Database and Spectral Simulation, 2.0	SRI International	https://www.sri.com/platform/lifbase-spectroscopy-tool/

RESOURCE AVAILABILITY

Lead contact

Requests for further information and resources should be directed to the lead contact, Guixin Zhang (guixin@mail.tsinghua.edu.cn).

Materials availability

This study did not generate new unique reagents.

Data and code availability

The data supporting the findings of this study are available from the corresponding author/lead contact upon reasonable request.

EXPERIMENTAL MODEL AND SUBJECT DETAILS

AMP generator

The AMP generator, with the dimensions of 68 cm × 16 cm×10 cm, consists mainly of a waveguide (WR-340) that includes an incident cavity, a circulator, a directional coupler, and a field applicator, as depicted in Figure 1A. A household magnetron operating at 2450 MHz was used to generate an electromagnetic field. This field enters the waveguide through the incident cavity and creates a stable standing wave state within the waveguide. The power output of the source (SM1250, Richardson Electronics, USA) can vary between 0 and 4.5 kW. The circulator and its water load protected the magnetron from reflected microwaves.[22] The absorbed power delivered to the AMP was measured using a directional coupler. The plasma was sustained within a vertically oriented quartz tube with an inner diameter and length of 26 mm and 40 cm, respectively. The tube was positioned at the standing wave peak with the high electric field, i.e., approximately $^{1}/_{4}^{th}$ of the wavelength of the waveguide away from the shorted end.

Through electromagnetic simulation and experimental optimization, we reduced the height of the field applicator to 23 mm near the quartz tube, thereby increasing the microwave energy density. Additionally, a temporary carbon coil was introduced into the quartz tube within the waveguide to increase the local electric field strength. The reduced waveguide and the carbon coil considerably increased the local electric field augmentation near the tube wall, as shown in Figure 1B. The carbon coil directly vaporized upon excitation due to microwave absorption and bombardment of seed particles, eliminating contamination during material synthesis. This enhancement significantly mitigated the challenges associated with the generation of an AMP. To maintain and stabilize the uniformity of the plasma, a swirling flow unit was employed to convert the directional feed gas into a swirling flow inside the quartz tube. This swirling flow additionally shielded the quartz tube from potential high-temperature damage.

Under atmospheric pressure, various gases can be ionized to create a microwave plasma that is homogeneous, stable, and has a large volume. Air and nitrogen are likely to be extensively utilized as carrier gases in future microwave plasma industrial applications due to their abundance, low cost, and ability to meet the requirements of practical industrial production. We selected ordinary air and nitrogen as the working gases and investigated the uniformity and gas temperature distribution of the AMP in both the radial and lateral directions, as shown in Figures 1C–1E. The conditions of the absorbed microwave power and gas flow rate were 1715 W and 12 L/min, respectively. The bottom views of the air and nitrogen AMPs were captured using a high-speed camera (Miro M310, Phantom, USA) with an exposure time of 80 μs, as shown in Figure 1C and the supplementary material. A side view of the AMPs beyond the waveguide was obtained, as shown in Figure 1D. The

total column length of the AMPs (including the internal waveguide part) can exceed 40 cm Figures 1C and 1D exhibit remarkably homogeneous large-volume profiles of the AMPs, with a volume of $\sim 10^2$ cm^3. Moreover, lowering the microwave frequency from 2450 MHz to 915 MHz resulted in a more than 10-fold increase in the volume (up to 10^4 cm^3) of the AMPs.

Materials and conditions

The optical parameters were measured from images and spectra of the plasma. A grating spectrometer (Princeton PI-Acton-SP2500i) was used in the spectral acquisition. A CCD (PIXIS 400) was mounted at the exit of the spectrometer to convert the acquired optical signals into electrical signals, which were output to a personal computer. The exposure time of the CCD was set to 1 s. Although the flow instability was thus time-averaged and the local, time-dependent spectrum was likely distorted at the above exposure time, the obtained spectra were the closest to the theoretical OH spectrum, with the smallest error among multiple attempts. The focal length of the spectrometer was 500 mm. The spectrometer was equipped with a 2400 lines/mm grating for measurement of spectra in a narrow wavelength range. The resolution of the grating, slit width of the spectrometer and instrumental broadening were 0.01 nm, 100 μm and 0.07 nm, respectively. A convex lens with a diameter of 5 mm and a focal length of 10 mm could be moved along a guide rail to collect the light from the plasma.

During the experiment, the spectra of the microwave plasma were measured from the bottom and from the side. At the bottom of the plasma torch, a collimation lens (74-UV) with a diameter of 200 μm was fixed to the optical fiber to collimate the input optical path into a parallel path, thus reducing the divergence angle of the optical fiber. The diameter and focal length of the lens were 5 mm and 10 mm, respectively. The collimation lens was moved along a guide rail (from $r = -8$ to 8 mm) to collect the radial spectra of the plasma. Using the single-mode optical fiber, the divergence angle θ was estimated from the Gaussian intensity distribution using $\theta \approx D/f \times 57.596^\circ \approx 1.15^\circ$, where D is the mode field diameter and f is the focal length of the collimator. For the measurements from the side of the plasma torch, the focus lens had the same parameters as the collimator lens. However, the distance between the focus lens and the optical fiber was decreased to allow light from a small spot in the central cross-section of the plasma torch to be focused into the fiber.

Using optical emission spectroscopy, the gas temperature in the plasma core was determined, while thermocouples were employed to measure the gas temperature in the outer plasma shell outside the waveguide.

A high-speed camera (Miro M310; Phantom, USA) with a lens (AF-S DX Micro NIKKOR 40 mm f/2.8G; Nikon, Japan) was used to capture the images, whose focus and aperture values could not be adjusted. The distance from the high-speed camera to the core area of the plasma was approximately 60 cm, which was much greater than the length of the plasma core (<5 cm). Therefore, the focal length of the lens did not affect the brightness of the plasma image obtained.

To validate the use of this large-volume, high-temperature source in material synthesis, we employed a vertically arranged N_2 AMP to consecutively synthesize silicon nanoparticles, graphene, and graphene-coated ferrosilicon core-shell (graphene@Si–Fe) composite nanoparticles in dozens of milliseconds. These materials require a high synthesis temperature and are economically valuable in energy storage applications; however, achieving high-quality and uncontaminated products by alternative means is challenging.[60–64] The precursors were 1 μm silicon powder, high-density polyethylene (PE) powder and a combination of ferrocene (40 wt. %) and silicon powder (60 wt. %), respectively. We used a powder doser (LAMBDA, Switzerland) to ensure that the the precursor powder fell to the plasma reaction zone at a uniform speed due to the effect of gravity and the rotational movement of a rod. The feed rate could be controlled precisely by adjusting the speed of the motor-driven rotating rod. The feed rate of the precursor powders was approximately 1 g/min for all experiments. In the experiments, the AMP was operated at an absorbed power of 2 kW with a nitrogen flow rate of 12 L/min. The practical plasma state during the synthesis process is shown in Figure 2A. The precursors were delivered into the AMP through the effect of gravity, and underwent vaporization and potential decomposition. This process results in the formation of atoms and radicals within wide regions of high-temperature and high-energy particles generated by the plasma. As the gaseous particles passed through the plasma core and moved away from it, they underwent supersaturation and precipitated due to a progressive decrease in the gas temperature. Inevitable frequent and stochastic collisions of these precipitated atoms resulted in homogeneous nucleation and subsequent growth, leading to the formation of the product materials. The AMP reaction process ensures the absence of any contamination in the product material due to the exceptional purity of the plasma used.

Raman spectroscopy: The formation of graphene was confirmed using Raman spectroscopy (LabRAM HR Evolution, HORIBA Jobin Yvon, Japan). The laser utilized in the experiment had a wavelength of 532 nm, a beam spot diameter of 1.25 μm and a power of 0.62 mW/cm^2. The scan time was 60 s, while the number of cumulative scans was one.

X-ray diffraction: XRD, D8 advance, Bruker, Germany.

Scanning electron microscopy: SEM, Merlin, Zeiss, Germany.

Transmission electron microscopy: TEM, JEM-2100F, JEOL, Japan.

METHOD DETAILS

Gas temperature measurement

Local thermodynamic equilibrium (LTE) is nearly reached in an atmospheric pressure microwave plasma flowing at a relatively low velocity (<120 m/s) because the convection rates are lower than those of the chemical reactions in this case.[23] In an LTE state, the gas temperature T_g is approximately equal to the rotational temperature of the atmospheric-pressure plasma due to its highly collisional nature and the nearly complete exchange of rotational and translational energy among the heavy species of the atmospheric-pressure plasma.[26] Since the lifetime of an OH radical molecule in the ground state is normally much longer than the characteristic time between collisions and the OH radical

spectrum is easily distinguished due to its small overlap with other spectral lines, the rotational temperature of the OH radical molecules usually provides a good representation of the gas temperature.[65]

In the high-temperature environment of the AMP, H_2O molecules are easily ionized into OH radicals. The emission spectrum of OH radicals via the $A^2\Sigma^+ \rightarrow X^2\Pi_r$ electronic band system is intense. This makes determination of the plasma gas temperature convenient. The OH radical spectrum is located mainly in the 305- to 325-nm wavelength region, and the relative intensities of its spectral lines are determined by the rotational and vibrational temperatures. In particular, the relative intensities of the spectral lines in the 306- to 310-nm wavelength region are determined almost exclusively by the rotational temperature.[66]

Therefore, we fitted the experimental spectra to the theoretical spectra of the $A^2\Sigma^+ \rightarrow X^2\Pi_r$ electronic system of OH radicals in the 306- to 310-nm band to obtain the AMP gas temperature. With the value of the maximum peak at 309 nm normalized to 100, the relative intensities of the other peaks within the 306- to 310-nm band were related almost solely to the rotational temperature. Moreover, the rotational temperature of the OH radical could be approximated as the gas temperature because intermolecular collisions frequently occur in microwave plasmas at atmospheric pressure.[65] Thus, the theoretical spectra could be fitted to the experimental spectra by adjusting the rotational temperature (varied at 10 K intervals) using LIFBASE spectral simulation software.[67] The best fit between the theoretical and experimental spectra was obtained when the sum of the variances between the experimental and theoretical spectra for all wavelength data points within the 306- to 310-nm band was minimized. When this best fit was achieved, the rotational temperature corresponding to the theoretical spectra could be considered the gas temperature of the microwave plasma. Figure S1 shows the best fit between the theoretical and experimental spectra at a rotational temperature T_r (i.e., gas temperature) of 5050 K.

Residence time estimation

Under the high temperature of the plasma, the precursor is considered to instantly vaporize; then, it transforms into the gaseous state in the plasma, and the flow rate is consistent with the plasma gas flow. Considering the effect of errors, similar to the 95% confidence interval used in statistics, the position where the brightness was 95% of the maximum brightness (i.e., a brightness of 243) was selected as the plasma boundary.

To simplify the analysis of the vortex gas flow, we can initially adopt the mean gas flow velocity $\overline{u}$ by neglecting the azimuthal component of $\vec{u}$, which is given by[68]

$$\overline{u} = \frac{Q}{\pi r^2}\frac{T_g}{300} \times \frac{1}{60} \times 10^{-3} \quad \text{(Equation 1)}$$

where Q is the gas flow rate in units of $L \cdot min^{-1}$, r is the inner radius of the quartz tube in units of m, and $\overline{u}$ is in units of $m \cdot s^{-1}$.

The residence time t, i.e., the duration over which nanomaterials transverse the plasma, can be estimated by dividing the axial length of the plasma by the mean gas flow velocity.